Supporting Information

Room Temperature Metallic Conductivity in a Metal-Organic Framework Induced by Oxidation

Andrew J. Clough,[a] Nicholas M. Orchanian,[a] Jonathan M. Skelton,[b] Abbey J. Neer,[a] Sebastian A. Howard,[c] Courtney A. Downes,[a] Louis F. J. Piper,[c,d] Aron Walsh,[e,f] Brent C. Melot,[a *] and Smaranda C. Marinescu[a] *

[a]Department of Chemistry, University of Southern California, Los Angeles, California 90089, United States

[b]Department of Chemistry, University of Bath, Bath BA2 7AY, United Kingdom

[c]Department of Physics, Applied Physics and Astronomy, Binghamton University, Binghamton, New York 13902, United States

[d]Materials Science & Engineering, Binghamton University, Binghamton, New York 13902, United States

[e]Department of Materials, Imperial College London, London SW7 2AZ, United Kingdom

[f]Department of Materials Science and Engineering, Yonsei University, Seoul 03722, Korea

* E-mail: smarines@usc.edu; melot@usc.edu.

General

All manipulations of air and moisture sensitive materials were conducted under a nitrogen atmosphere in a Vacuum Atmospheres drybox or on a dual manifold Schlenk line. The glassware was oven-dried prior to use. Acetonitrile and dichloromethane were degassed with nitrogen and passed through activated alumina columns and stored over 4 Å Linde-type molecular sieves. Ethyl acetate, water, and ethanol were placed under vacuum and refilled with nitrogen (10 ×). Deuterated solvents were dried over 4 Å Linde-type molecular sieves prior to use. Elemental analyses were performed by Robertson Microlit Laboratories, 1705 U.S. Highway 46, Suite 1D, Ledgewood, New Jersey, 07852. All the chemical regents were purchased from commercial vendors and used without further purification. The ligand 2,3,6,7,10,11-triphenylene-hexathiol[1] (THT) was prepared according to the reported procedures. Water was deionized with the Millipore Milli-Q Synergy system (18.2 MΩ·cm resistivity). All other chemical regents were purchased from commercial vendors and used without further purification.

Synthesis of FeTHT

The iron triphenylene-2,3,6,7,10,11-hexathiolate framework, **FeTHT**, was prepared according to the reported procedure for the analogous cobalt framework.[2,3] A 120 mL glass jar was charged with an aqueous solution of $FeCl_2 \cdot 4H_2O$ (40 mg, 0.21 mmol, 5 mM, 40 mL volume). Separately, a suspension of triphenylene-2,3,6,7,10,11-hexathiol (THT) (2 mg, 0.005 mmol) in N-Methyl-2-pyrrolidone (NMP) (0.2 mL) was diluted with ethyl acetate until the total volume of the suspension reached 20 mL, sealed, and briefly sonicated to form an uniform suspension. Ethyl acetate (40 mL) was gently added to the aqueous solution of iron(II) chloride to create a liquid-liquid interface. The suspension of THT and NMP was then gently added to the ethyl acetate

layer and the jar was sealed and allowed to stand. A black film appeared at the liquid-liquid interface over 5 days. The film was deposited onto glass supports by pulling the substrate through the film. The deposited films were subsequently washed with water and allowed to evaporate to dryness. Alternatively, the black solid of **FeTHT** was collected by filtration and washed with water and methanol for bulk powder analyses.
FeTHT powders or films were oxidized by placing them in an oven at 60 °C for 3 days. Anal. Calcd for $Fe_3(THT_{ox})_2 \bullet 3MeOH \bullet 12H_2O$ ($Fe_3C_{45}H_{48}S_{12}O_{44}$), where THTox = $C_{18}H_6O_9S_6$: C, 32.38; H, 2.62; Fe, 9.08; S, 23.05. Found: C, 32.89; H, 2.86; Fe, 9.28; S, 23.53.

Powder X-ray diffraction (PXRD) studies were performed on a Rigaku Ultima IV X-Ray diffractometer in reflectance parallel beam/parallel slit alignment geometry. The measurement employed Cu Kα line focused radiation at 1760 W (40 kV, 44 mA) power and a Ge crystal detector fitted with a 2 mm radiation entrance slit. Samples were mounted on zero-background sample holders and were observed using a 0.08° 2θ step scan from 2.0 – 40.0° with an exposure time of 0.4 s per step. No peaks could be resolved from the baseline for $2\theta > 35°$.

High resolution synchrotron powder X-ray diffraction data was collected using the 11-BM beamline mail-in program at the Advanced Photon Source (APS), Argonne National Laboratory, with an average wavelength of 0.414576 Å. Discrete detectors covering an angular range from 0.5 to 30º 2θ are scanned over a 34º 2θ range, with data points collected every 0.001º 2θ and scan speed of 0.01º/s. An Oxford Cryosystems Cryostream Plus device allowed for sample temperatures to be controlled over a range of 100-340 K.

Gas Sorption Measurements
Brunauer-Emmett-Teller (BET) measurements were performed on a Nova 2200e surface area and pore size analyzer (Quantachrome Instruments, Inc.). Samples were degassed for 3 days at 60 °C in vacuo prior to measurements.

Modeling
Molecular modeling of **FeTHT** was carried out using the Materials Studio (version 8.0) suite of programs by Accelrys. The molecular fragment used to generate the model is shown in Figure S1. The unit cell was constructed starting with a primitive hexagonal unit cell with space group P6/*mmm* using cell parameters $a = b = 22.52$ Å and $c = 3.3$ Å. The structure was optimized with Materials Studio Forcite calculations using geometry optimization and universal forcefield methods. The MS Reflex module was used to calculate the expected PXRD patterns. Line broadening for crystallite size was not calculated. Comparison of the simulated and experimental PXRD patterns verified the simulated structure.

Scanning Electron Microscopy (SEM)
SEM images of **FeTHT** on glass substrates were collected using a JEOL-7001F or FEI Nova NanoSEM 450 operating at 10 or 15 kV with 5 nA of probe current.

Conductivity Measurements
FeTHT films were deposited onto glass supports by pulling the substrate (glass) through the **FeTHT** film formed at the liquid-liquid interface, as described previously. The deposited films were subsequently washed with water and allowed to evaporate to dryness. Conductivity measurements were performed using a custom set up integrated into a 14T Quantum Design

Dynacool Physical Properties Measurement System. A Keithley 6220 Precision Current Source (excitation currents of 1-50 nA) was used to trigger and control a Keithley 2182A nanovoltmeter. In order to minimize errors associated with contact resistance and drift voltages, a Keithley 2172 matrix switch equipped with a Keithley 6536 Hall effect card was used to alternate the direction of the applied current. Because of difficulty associated with preparing samples with uniform dimensions, all measurements were performed in a four-point probe Van der Pauw geometry. Copper wire contacts were attached to the films using conductive carbon paint and soldered onto a Quantum Design puck with resistivity option. All measurements were performed under a reduced pressure of ~10 torr.

Magnetic Studies

Temperature-dependent susceptibility measurements of pristine FeTHT show a paramagnetic response down to 2 K, as illustrated in Figure S23a. A fit of the high temperature magnetic susceptibility (175–275 K) to the Curie-Weiss law $\chi = C/(T-\Theta_{cw})$ yields an effective paramagnetic moment, $\mu_{eff} = 2.20\ \mu_B$ per formula unit and a Curie-Weiss temperature Θ_{cw} of 0.60 K. The fit, shown in Figure S23b, shows a slight positive deviation corresponding to the positive Θ_{cw} of 0.60 K, which indicates that the dominant exchange interaction among the Fe ions is slightly ferromagnetic. During magnetization, the sample does not saturate up to 14 T (Figure S23c), which is characteristic of a paramagnetic material.

Atomic Force Microscopy (AFM)

FeTHT films were deposited onto glass supports by pulling the substrate (glass) through the **FeTHT** film formed at the liquid-liquid interface, as described previously. The deposited films were subsequently washed with water and allowed to evaporate to dryness. AFM topography images were collected in tapping mode using an Agilent 5420 SPM instrument operating in tapping mode. The probe tips were Tap300-G Silicon AFM probes (resonant frequency 300 kHz, force constant 40 N/m) purchased from Budgetsensors.com and aligned prior to use. Images were collected with a scan rate of 0.1 lines per second and over an area of 40 μm. All samples were imaged under one atmosphere of air at room temperature.

X-Ray Photoelectron Spectroscopy (XPS)

Care was taken to reduce additional air exposure of the **FeTHT** samples by mounting in a glovebox with an argon environment and transferring via sealed vacuum suitcase to a lab-based XPS with a monochromatic Al-Kα source and hemispherical analyzer located at the Analytical and Diagnostics Laboratory at Binghamton University. Measurements were performed at room temperature with a pass energy of 23.5 eV, corresponding to an instrumental resolution of 0.51 eV, determined from analyzing the Fermi edge and Au $4f_{7/2}$ peak of gold foil references. Lorentzian broadening of Fe 2p multiplet peaks, necessary to fit Voight profiles in peak fitting, was approximated from the instrumental resolution and FWHM of Fe_3O_4 peaks.[4] Energy calibration of all core regions were made to Au $4f_{7/2}$ peak(84.0 eV) of gold foil references.

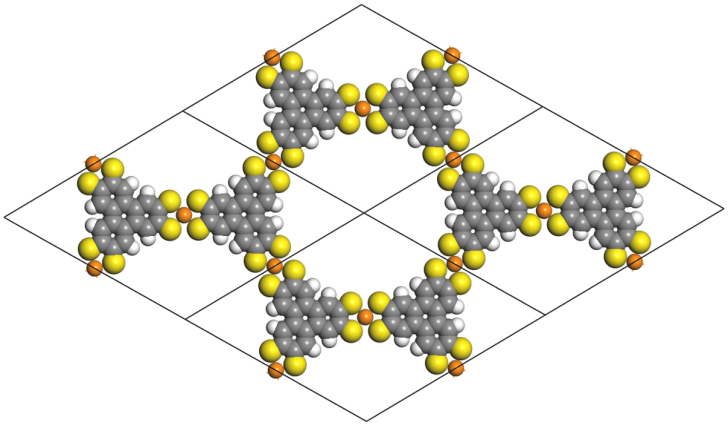

Figure S1. Spacefilling model of the fragment used to generate the unit cell of **FeTHT**.

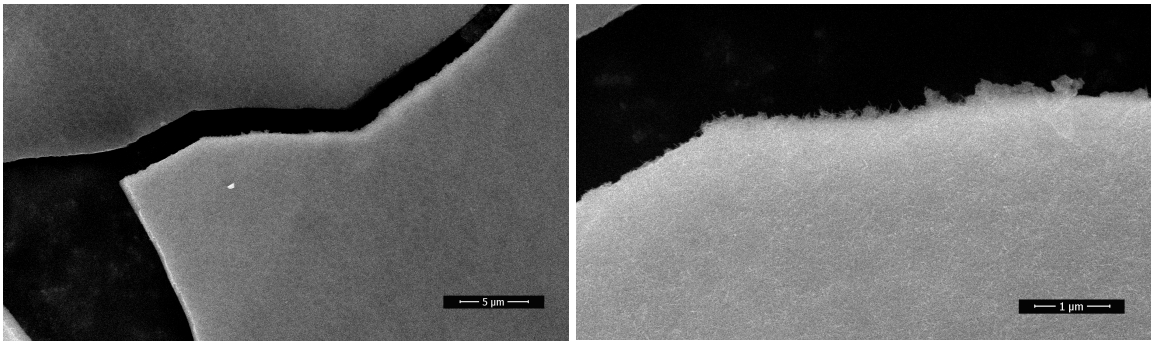

Figure S2. SEM images of **FeTHT**.

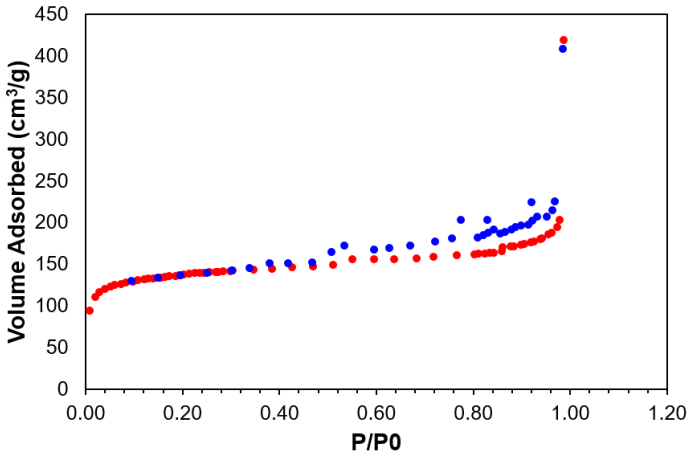

Figure S3. Nitrogen sorption isotherms performed on the as-prepared **FeTHT** at 77 K reveal a BET surface area of 441 m^2/g.

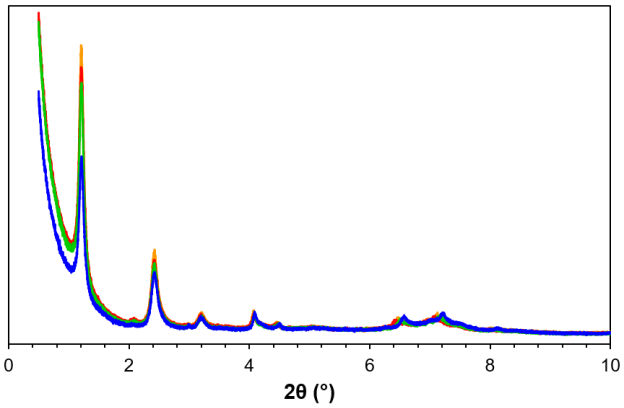

Figure S4. Overlay of the variable temperature PXRD patterns of an oxidized **FeTHT** sample exposed to air for 3 days at 60 °C. Data was collected at 100 (blue), 200 (green), 295 (orange), and 340 (red) K.

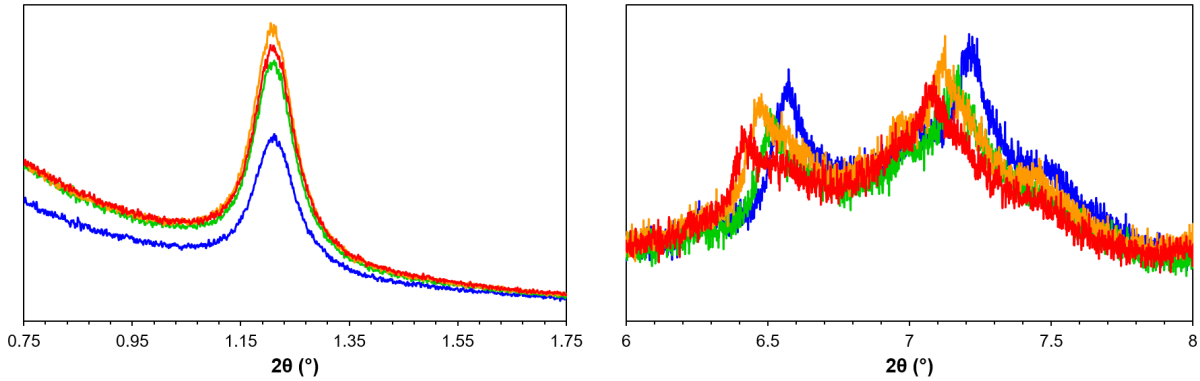

Figure S5. Overlay of the variable temperature PXRD patterns of an oxidized **FeTHT** sample exposed to air for 3 days at 60 °C, focusing on the [100] (left) and [001] (right) reflections. Data was collected at 100 (blue), 200 (green), 295 (orange), and 340 (red) K.

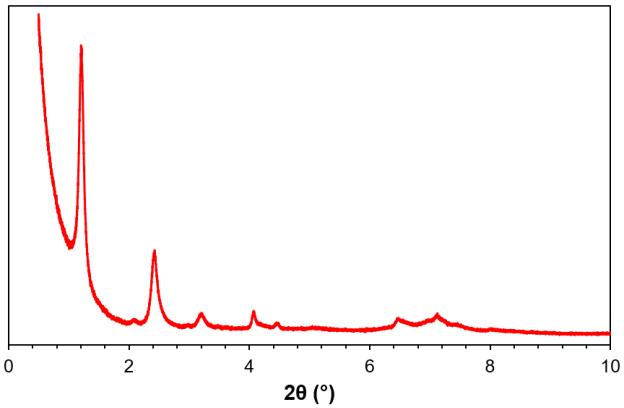

Figure S6. PXRD pattern of an oxidized **FeTHT** sample exposed to air for 3 days at 60 °C. Data was collected at 295 K.

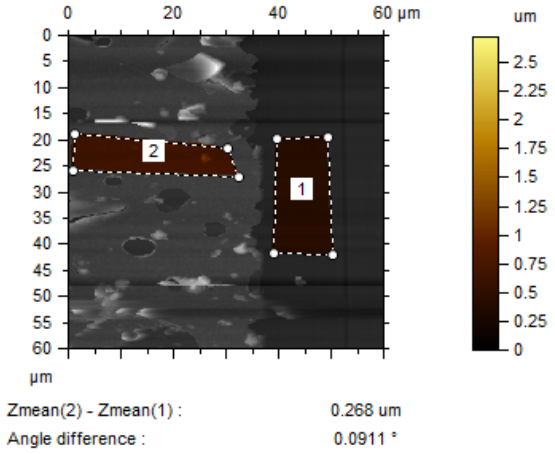

Figure S7. Atomic Force Microscopy (AFM) studies of an oxidized **FeTHT** sample exposed to air for 3 days at 60 °C. The measured film thickness is 275(28) nm.

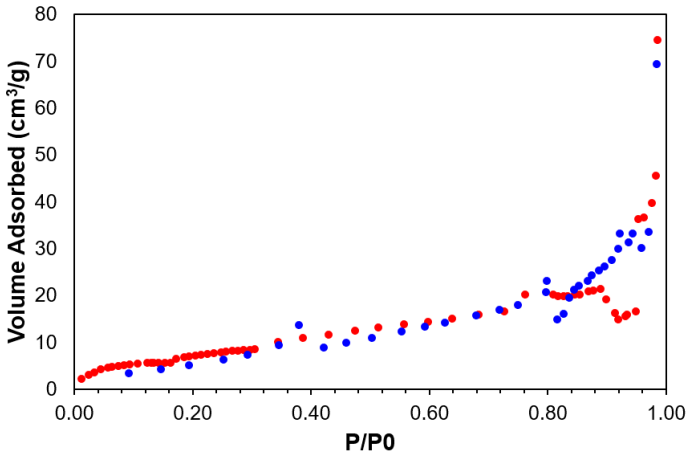

Figure S8. Nitrogen isotherms performed on an oxidized **FeTHT** sample exposed to air for 3 days at 60 °C. Data collected at 77 K after air-exposure reveal a BET surface area of 27.6 m^2/g (red: adsorption, blue: desorption).

Computational Modelling

Periodic density-functional theory (DFT) calculations on the **FeTHT** framework were carried out within the pseudopotential plane-wave formalism implemented in the Vienna *Ab initio* Simulation Package (VASP) code.[5]

Electron exchange and correlation were modelled with the PBEsol functional[6] with the DFT-D3 dispersion correction[7] (i.e. PBEsol-D3). A subset of calculations were repeated with a Hubbard correction of U_{eff} = 5 eV applied to the Fe d states using the Dudarev method.[8]

The ion cores were modelled using projector augmented-wave (PAW) pseudopotentials[9,10] with the H 1s, C 2s/2p, S 3s/3p and Fe 4s, 3d and 3p electrons included in the valence shells. Based on our previous studies of the analogous Co framework,[3] an 800 eV kinetic-energy cutoff was employed for the plane-wave basis and the electronic wavefunctions were modelled using a Γ-centred Monkhorst-Pack *k*-point mesh[11] with 1×1×5 subdivisions, reduced appropriately for supercell calculations. A Gaussian smearing of 0.01 eV was used to determine partial band occupations.

Tolerances of 10^{-8} eV and 10^{-2} eV $Å^{-1}$ were applied to the total energy and forces during minimisation of the electronic wavefunctions and geometry optimisations, respectively. The precision of the charge-density grids was set to avoid aliasing errors and the PAW projection was performed in real space.

The electronic density-of-states (DoS) curves were evaluated from a single-point calculation with an increased *k*-point density of 2×2×15 subdivisions and a larger smearing width of 0.05 eV. The charge density from these calculations was then used to model band dispersions by calculating the eigenvalues on strings of *k*-points along high-symmetry directions in the Brillouin zone non self-consistently.

Equilibrium Geometry and Magnetic Structure

To identify the most energetically-favourable magnetic configuration, we made a starting assumption of a 50/50 mixture of Fe^{2+} and Fe^{3+} ions in a square-planar crystal field with zero and one unpaired electron, respectively. A 50/50 mixture of charge states is not compatible with the three Fe ions in the crystallographic primitive unit cell of the **FeTHT** framework, so we constructed trial magnetic unit cells based on 1×1×2 and 2×2×1 expansions of the primitive cell with 6/12 Fe ions and enumerated all symmetry-inequivalent arrangements of the Fe^{2+} and Fe^{3+} ions using the Transformer code,[12] yielding in a total of three and 30 initial configurations in the two cells, respectively. A single-point energy calculation was then carried out on each model, with the magnetic moments allowed to relax during the optimisation of the electronic wavefunctions. We note that this is a more systematic approach than that taken in our previous study on the cobalt analogue (**CoTHT**).[3]

All 33 initial models relaxed to configurations with magnetic moments around ±2 BM per Fe ion, consistent with all the ions adopting the Fe^{3+} oxidation state. The calculations on the 1×1×2 supercell produced one ferromagnetic and one frustrated antiferromagnetic configuration with total moments of 6.3 and 2.0 BM per formula unit (i.e. per single unit cell), respectively. The latter configuration is calculated to be 20 meV per Fe ion lower in energy than the fully ferromagnetic arrangement and is based on chains of Fe ions with parallel spin along the *c* axis and a mix of ferromagnetic and antiferromagnetic coupling between chains within the layers. A configuration constrained to have ferromagnetic interlayer and antiferromagnetic intralayer coupling was found to be ~0.1 eV per ion higher in energy than the fully ferromagnetic configuration, indicating a strong preference for ferromagnetic coupling between layers.

The majority of the 30 2×2×1 models relaxed to antiferromagnetic ground states with an equal number of both spin states, but a small number adopted configurations with two and four excess spins and net magnetic moments of 1.1 and 2.2 BM per formula unit, respectively. The

energetic differences were on the order of 1-2 meV per Fe ion, suggesting weak intralayer coupling.

Three of the initial screened configurations were selected for full geometry optimisation, *viz.* the frustrated antiferromagnetic 1×1×2 expansion (Model 1), the antiferromagnetic 2×2×1 expansion (Model 2), and the 2×2×1 expansion with the larger magnetic moment of 2.2 BM per formula unit (Model 3). The optimised lattice parameters, total magnetic moments and total energies are compared in Table S1.

	Expt.	Model 1	Model 2	Model 3
Supercell	-	1×1×2	2×2×1	2×2×1
a [Å]	22.52	23.23	23.22	23.22
c [Å]	3.3	3.299	3.256	3.335
c/a	0.147	0.142	0.143	0.144
V [Å^3]	1449	1541	1553	1557
M [BM]	1.87	3.04	-0.03	2.21
E_0 [eV per Fe ion]	-	-155.24	-155.30	-155.30

Table S1. Optimised lattice parameters, total magnetic moments and total energies of three trial magnetic supercells of the **FeTHT** framework. The lattice parameters and magnetic moments are given with respect to the crystallographic unit cell (i.e. containing three Fe ions), and the total energies are given per Fe ion. The experimental values are shown in the second column for comparison.

Given the weak intralayer coupling, the 1×1×2 and net magnetic 2×2×1 configurations (Models 1 and 3) should be roughly equivalent, and the differences in Table 1 provide an estimate of how much variation can be expected due to differences in the choice of unit cell and associated technical parameters such as the *k*-point sampling. With this in mind, the only major difference between all three models is the magnetic moment. Since Models 1 and 3 can be represented to some level of approximation with a single crystallographic unit cell, which is much more computationally tractable than either supercell, we opted to do this in our production calculations. This also has the advantage of making the calculations directly comparable to those in our previous work on the **CoTHT** analogue.[3]

Using the single-cell configuration, we obtained optimised lattice parameters of a = 23.21 and c = 3.334 Å, which are a good match to the experimental measurements of 22.52 and 3.3 Å respectively. The calculated spin density (Figure S9) shows that the unpaired electrons are

localised to the Fe d orbitals, as expected, with a small amount of density on the coordinating S atoms and very little on the ligand π system.

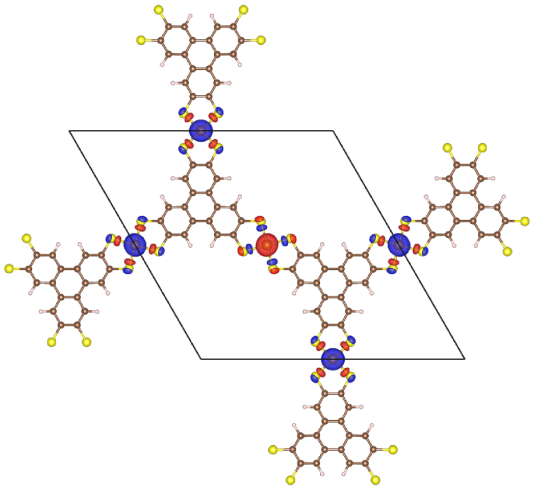

Figure S9. Spin density of the lowest-energy magnetic configuration of the **FeTHT** framework.

With the more accurate convergence settings used in the electronic-structure calculations, we obtain a magnetic moment of 2.15 BM per formula unit, which is very close to the low-temperature experimental measurement of 2.2 BM, albeit with a different origin. We also note that the weak intralayer coupling predicted by the calculations would, in principle, allow the system to adopt alternative spin configurations at finite temperature or in response to perturbations to the crystal field, for example oxidation, which is again consistent with experimental observations.

Electronic Structure

Figure S10 shows the band dispersion and electronic density of states (DoS) curves calculated for the **FeTHT** framework. As for the **CoTHT** analogue, the calculations predict this system to be a semi-metal, with a cluster of bands crossing the Fermi energy along the Γ-*A* direction in reciprocal space. This corresponds to the *c* direction in real space, and an orbital-density plot of the states within 25 meV of the Fermi energy (Figure S11) shows that that the partially-occupied bands in both frameworks correspond primarily to chains of interacting Fe and S orbitals with a small contribution from the ligand π system.

As in our previous study, bands crossing the Fermi energy were identified and the one-dimensional $E(k)$ dispersion relation fitted to a quadratic function to estimate the carrier effective masses according to:[3]

$$\frac{1}{m^*} = \frac{1}{\hbar^2}\frac{\partial^2 E(k)}{\partial k^2} \quad (1)$$

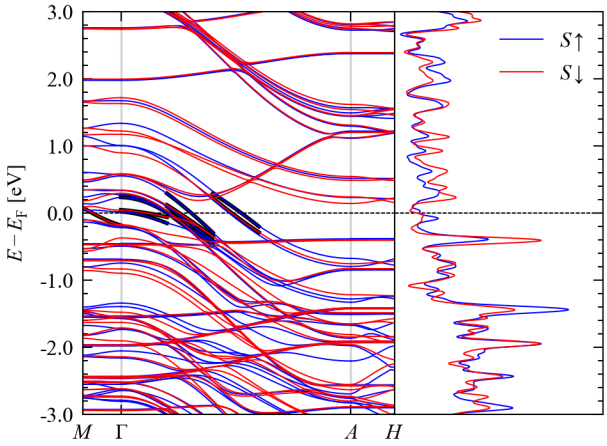

Figure S10. Calculated band dispersion and electronic density of states curves for the **FeTHT** framework. The blue and red lines denote electronic states in the "up" and "down" spin channels. The thick black lines indicate the parts of the dispersion used to evaluate $\partial^2 E(k)/\partial k^2$ for estimating the carrier effective masses.

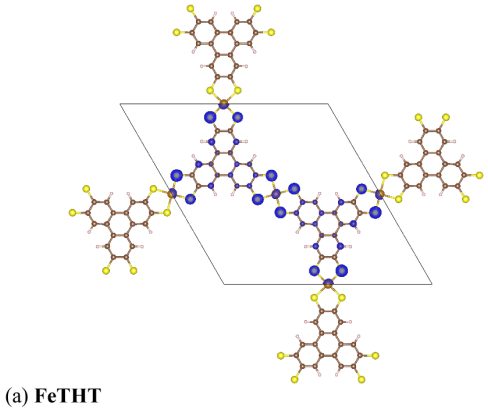

(a) **FeTHT**

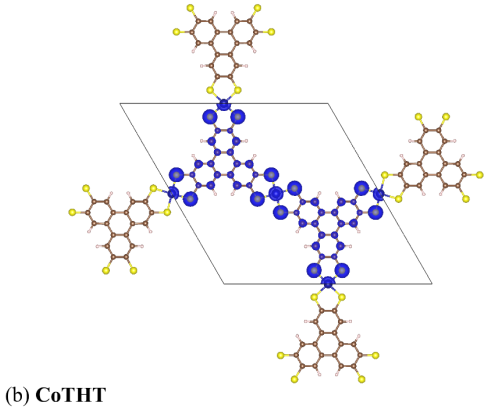

(b) **CoTHT**

Figure S11. Orbital density showing states within 25 meV of the Fermi energy in the **FeTHT** (a) and analagous **CoTHT** (b) framework studied in our previous work (Ref.[3]).

The relatively large bandwidth of up to ~1.8 eV results in low carrier effective masses of -0.55 to -6.72 and 1.36 to 2.78 m_e, which can be compared to masses of -0.42 to -1.52 and 0.29 to 8.04 m_e in **CoTHT**.[3] Some of the bands along the *M*- Γ segment, corresponding to in-plane conductivity, are also metallic, with a carrier mass around 0.99.

Stacking Faults

Previous studies on the layered $Ni_3(HITP)_2$ framework (HITP = 2,3,6,7,10,11-hexaiminotriphenylenesemiquinonate) showed this system to preferentially adopt a staggered layer arrangement.[13] In contrast, however, our previous study on **CoTHT** found that an eclipsed layer configuration was the most energetically favourable.[3]

To examine the layer stacking in the **FeTHT** framework, we carried out a similar study to explore the potential-energy surface associated with the relative positions of the layers in a bilayer 1×1×2 supercell expansion (Figure S12). As in our previous work, a series of single-point calculations were performed with one layer displaced relative to the other by up to 4 Å

along the *a* and *b* axes, and at each (Δa, Δb) displacement coordinate the energies of interlayer spacings from 3.084 to 3.584 Å were calculated and the minimum obtained from a polynomial fit (see Figure S13).

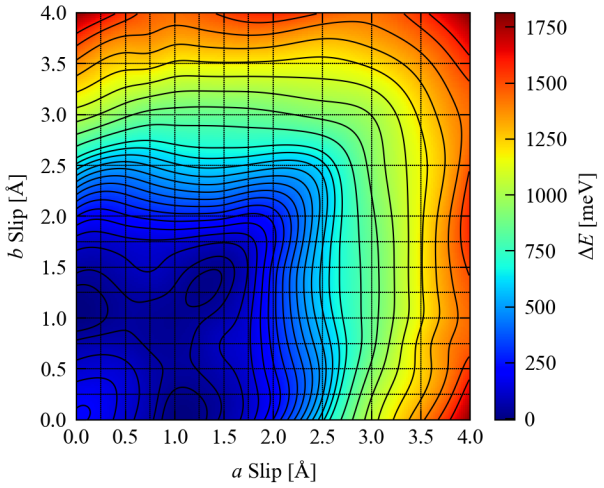

Figure S12. Calculated potential-energy surface associated with layer offsets in the **FeTHT** framework.

In contrast to the Co analogue, the fully eclipsed configuration of the **FeTHT** framework is 0.21 eV (34 meV per Fe ion) higher in energy than the global minima, which correspond to displacements along the *a* or *b* directions of $\Delta \approx 1.0$-1.25 Å. There is also a secondary local minimum located close to $\Delta = (1.25, 1.25)$ which is a very small 14 meV (2.4 meV per Fe ion) higher in energy. To investigate further, the two global minima and the low-lying local minimum were fully volume relaxed. Figure S14 shows a view along the *c* axis of each of the three staggered bilayer structures, and the lattice parameters, magnetic moments and total energies are compared to those of an eclipsed bilayer configuration in Table S2.

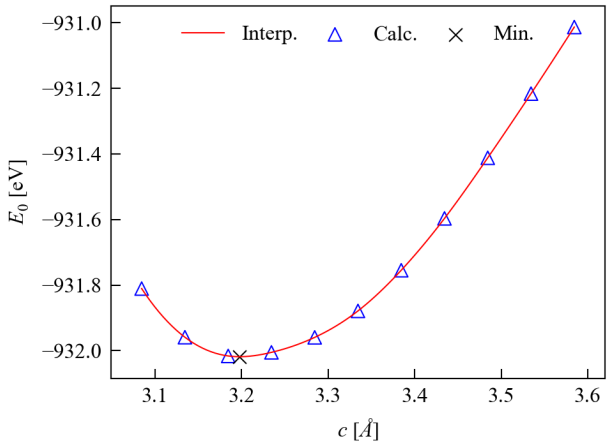

Figure S13. Illustration of the procedure for locating the minimum-energy *c*-axis length (interlayer spacing) at a layer displacement of Δa = 1.25 and Δb = 1.25 Å. The blue markers show the calculated total energies, the red line shows a 1D cubic spline interpolation through the data, and the cross marks the position of the identified energy minimum.

	Expt.	Eclipsed	(1.00, 0.00)	(0.00, 1.00)	(1.25, 0.25)
a [Å]	22.52	23.210	23.226	23.226	23.218
c [Å]	3.3	3.334	3.159	3.159	3.163
c/*a*	0.147	0.150	0.136	0.136	0.136
V [Å^3]	1449	1556	1476	1475	1476
M [BM]	1.87	2.17[a]	2.11	2.11	1.71
E_0 [eV per Fe ion]	-	-155.30[a]	-155.39	-155.39	-155.40

Table S2. Optimised lattice parameters, total magnetic moments and total energies of the **FeTHT** framework with eclipsed layers and the three different staggered layer configurations (stacking faults) shown in Figure S14. As in Table 1, The lattice parameters and magnetic moments are given with respect to the crystallographic unit cell, and the total energies are given per Fe ion. The experimental values are shown in the second column for comparison.[a] Values computed for a 1×1×2 expansion of the optimised single-cell model.

After optimisation, the staggered minima are further lowered in energy to 83 meV per Fe ion relative to the eclipsed configuration. The structure displaced along both the *a* and *b* axes (Figure S14c) becomes the global minimum, being a comparatively small 15 meV per Fe ion

lower in energy than the two structures displaced along one of the in-plane directions. All three staggered configurations result in a slight expansion of the *a* and *b* axes by 0.01-0.02 Å and a contraction of the *c* axis by 0.17-0.18 Å (5.2 %), which together produce a 5 % reduction in the unit-cell volume. The layer offsets do not appear to change the magnetic ordering, but the calculations predict that simultaneous displacement along both *a* and *b* axes could reduce the total magnetic moment by up to ~20 %.

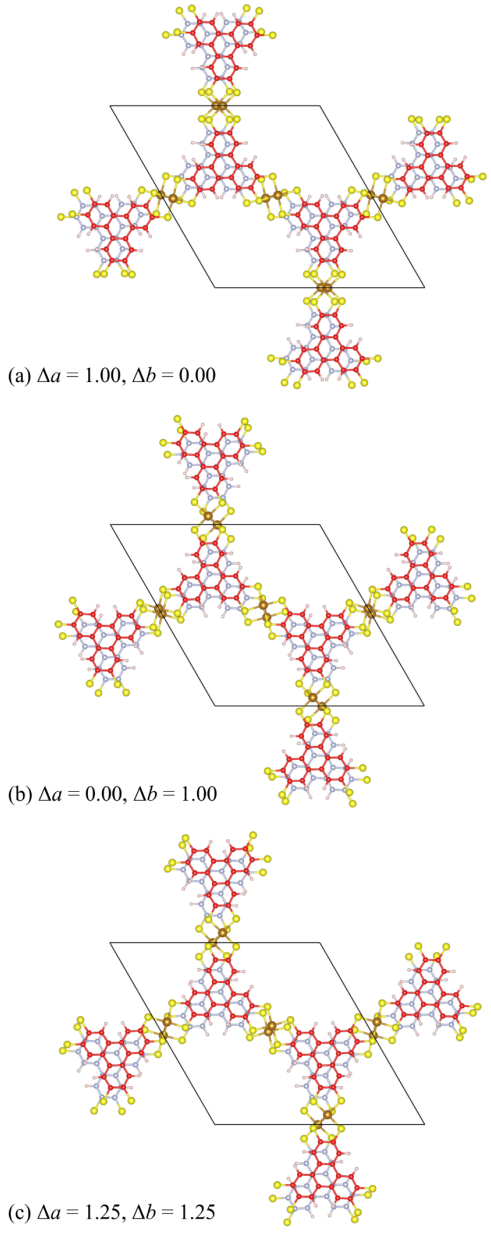

Figure S14. Optimised structures of bilayer models of **FeTHT** with layer displacements corresponding to the local minima in Fig. 4, *viz.* Δ = (1.00, 0.00) (a), Δ = (0.00, 1.00) (b) and Δ =

(1.25, 1.25) (c). For clarity, the carbon skeletons of the THT ligand in the two layers are coloured red and blue.

The layer displacement has a small effect on the calculated electronic structure (Figure S15), in particular opening a gap in the conduction band at ~1 eV above the Fermi energy, which is similar to the effect of increasing the interlayer spacing in the **CoTHT** analogue.[3] To quantify the changes in the density of states around the Fermi energy, we estimated the room-temperature (T = 300 K) concentration of conduction electrons according to:

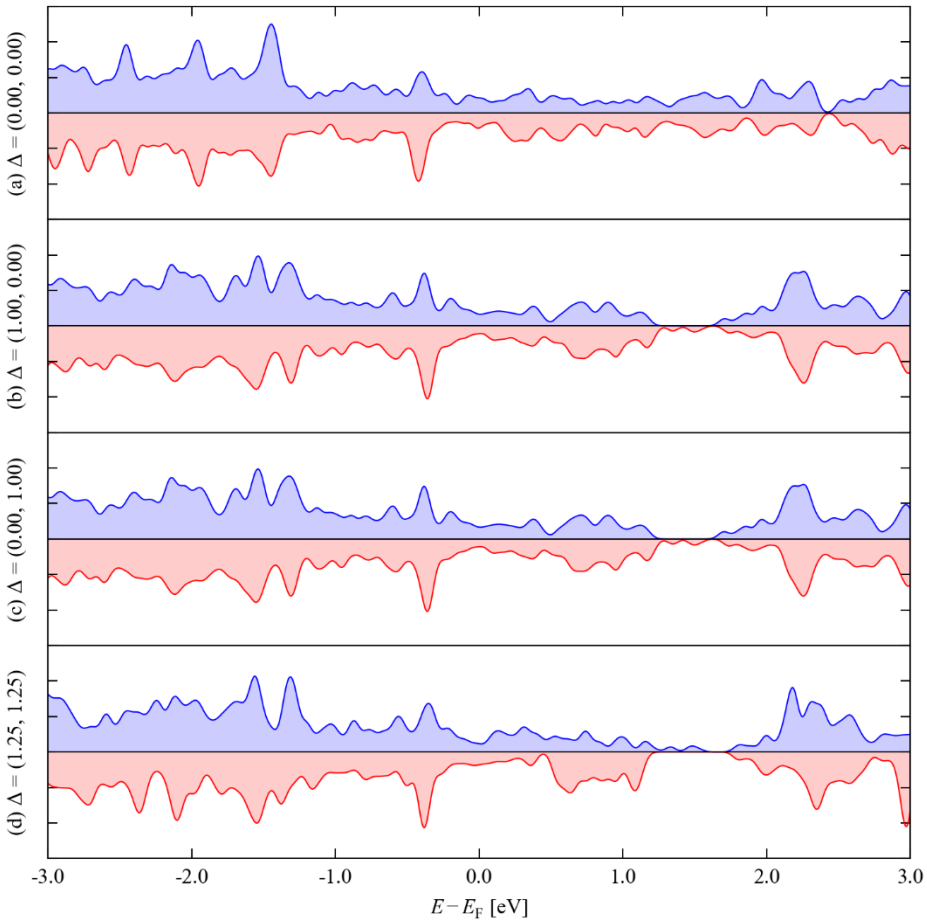

Figure S15. Electronic density of states (DoS) curves of bilayer models of **FeTHT** in the eclipsed configuration (a) and staggered configurations corresponding to displacements along the *a* and *b* axes of Δ = (1.00, 0.00) (b), Δ = (0.00, 1.00) (c) and Δ = (1.25, 1.25) (d). The positive and negative curves on each subplot denote the DoS in the "up" (blue) and "down" (red) spin channels.

$$n_e(T) = \int_{E_F}^{E_{max}} f(E)g(E)dE = \int_{E_F}^{E_{max}} \frac{1}{1 + \exp\left(\frac{E - E_F}{k_B T}\right)} g(E)dE \quad (2)$$

where $f(E)$ is the Fermi-Dirac distribution, $g(E)$ is the electronic density of states, k_B is the Boltzmann constant and the integral runs from the Fermi energy to the highest-energy conduction states in the calculations. We obtained a value of 8.8×10^{25} m^{-3} for the eclipsed structure, which, compared to a typical value of 10^{28} m^{-3} for a "good" metal, supports the predicted semi-metallic nature of the **FeTHT** system. The calculated concentrations of 7.2×10^{25} and 7.5×10^{25} m^{-3} for the structures with layers displaced along the *a*/*b* and both axes, respectively, suggest that layer misalignment reduces the density of conduction states close to the Fermi energy, as would be expected given the nature of the conductive states (c.f. Figure S6). This result is again similar to the behaviour of the **CoTHT** analogue.[3]

These results indicate that the **FeTHT** system may show a propensity for layer misalignment, in contrast to the **CoTHT** analogue, and the effect of this, together with environmental factors such as the presence of guest molecules in the pores, may play a role in the measured temperature dependence of the resistivity.

Effect of a Hubbard U Correction

Systems with strongly-localised electrons, such as those containing d- and f-block elements, can pose a challenge to (semi-)local DFT methods such as PBEsol, where self-interaction error tends to overly delocalise the electrons and predict unrealistic electron energies and other calculated physical properties such as the magnetic ground state.[14] Of particular importance to this work is that in some systems the error can lead to calculations predicting insulators to be metals.[15] A straightforward and computationally-efficient method to correct for self-interaction is to apply a Hubbard *U* correction to specific atomic states and introduce an energy penalty to force the orbital occupations towards integer values.[8,14]

To test the effect of a Hubbard correction on our results, we performed an identical set of calculations on the single-cell model of the **FeTHT** framework with a Hubbard correction of U = 5 eV applied to the Fe d states. This resulted in a slight lengthening of the *a* and *c* lattice constants by ~0.1 Å and a 1 % increase in the cell volume (Table S3). The frustrated antiferromagnetic configuration holds, but stronger localisation of the Fe d electrons increases the total magnetic moment from 2.2 to 2.4 BM per F.U., with the individual Fe moments increasing from $\pm$2.0 to $\pm$2.8 BM per ion. The correction leads to noticeable changes in the electronic structure (Figure S16), but the semi-metallic nature of the framework is preserved, and the carrier effective masses obtained from the curvature of bands along the *M*-Γ and Γ-*A* directions are of comparable magnitude to the bare DFT values, albeit with larger variation and heavier extremes.

Similar DFT+*U* calculations on the **CoTHT** analogue with an identical correction of U = 5 eV applied to the Co d states gave similar results (Table 4, Figure S17), leading to expansion of the *c* axis by ~0.3 Å, a 9.5 % increase in the cell volume, and an increase in the total and Co magnetic moments from 2.2 to 4.8 BM per F.U. and 2.0 to 2.8 BM per Co ion, respectively. The larger changes compared to the **FeTHT** framework could be due to the predicted fully-ferromagnetic ground state in the Co framework, although systematic studies on transition-metal oxides suggest that the Co system may not need as large a U value as the Fe one.[16] Once again, despite noticeable changes to the electronic band dispersion and DoS, the predicted semi-metallic electronic structure is preserved, and the calculated carrier effective masses are of a similar magnitude.

These calculations provide some confidence that the predicted semi-metallic electronic structure of the pristine framework is not an artefact from our use of the semi-local PBEsol exchange-correlation functional, although we note that more sophisticated treatments of electron correlation may produce a different picture. However, we consider such an undertaking to be beyond the scope of this investigation.

		Calc.	
	Expt.	PBEsol-D3	PBEsol-D3 + U
a [Å]	22.52	23.210	23.308
c [Å]	3.3	3.334	3.342
c/a	0.147	0.150	0.143
V [Å^3]	1449	1556	1572
M [BM]	2.20	2.15 (1.95, 1.95, -1.95)	2.43 (2.83, 2.83, -2.83)

Table S3. Calculated lattice parameters and magnetic moments of the **FeTHT** framework structure obtained using the PBEsol-D3 functional with and without a Hubbard correction of U = 5 eV applied to the Fe d states. For each calculation, both the total magnetic moment and the moments of the three Fe ions are given. Experimental values are shown in the second column for comparison.

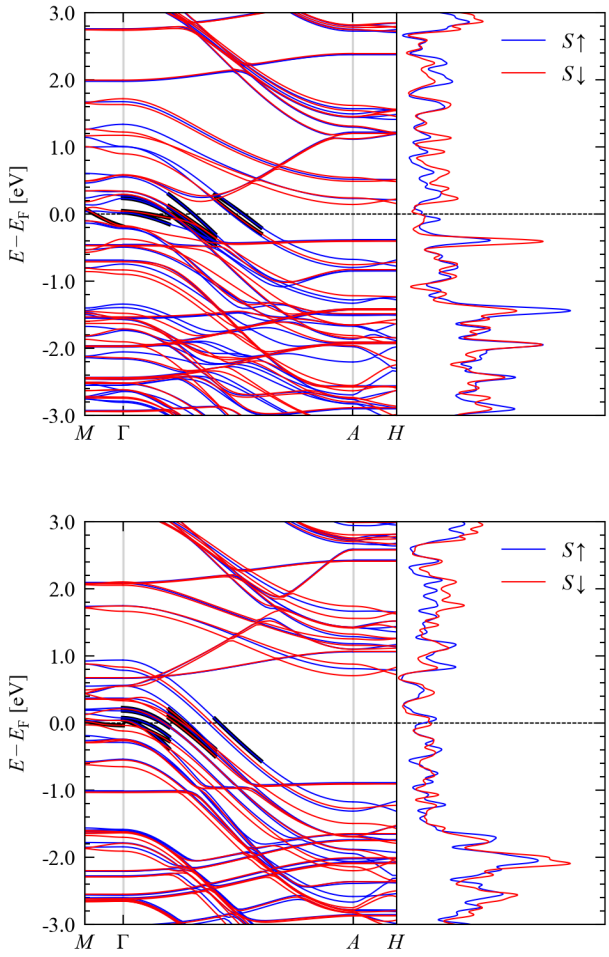

Figure S16. Band dispersion and electronic density of states (DoS) curves of the **FeTHT** framework calculated with PBEsol (top) and PBEsol+*U* with a Hubbard correction of *U* = 5 eV applied to the Fe d states (bottom). As in Figure S5, the blue and red colours denote electronic states in the two spin channels, and the thick black lines indicate parts of the dispersion used to evaluate $\partial^2 E(k)/\partial k^2$ for estimating the carrier effective masses.

		Calc.	
	Expt.	PBEsol-D3	PBEsol-D3 + *U*
a [Å]	22.52	23.133	23.135
c [Å]	3.3	3.140	3.438
c/*a*	0.147	0.136	0.149
V [Å^3]	1449	1455	1593
M [BM]	1.87	2.15 (0.66, 0.67, 0.66)	4.77 (1.81, 1.81, 1.81)

Table S4. Calculated lattice parameters and magnetic moments of the **CoTHT** analogue of the **FeTHT** framework obtained using the PBEsol-D3 functional with and without a Hubbard correction of U = 5 eV applied to the Co d states. For each calculation, both the total magnetic moment and the moments of the three Co ions are given. Experimental values are shown in the second column for comparison.

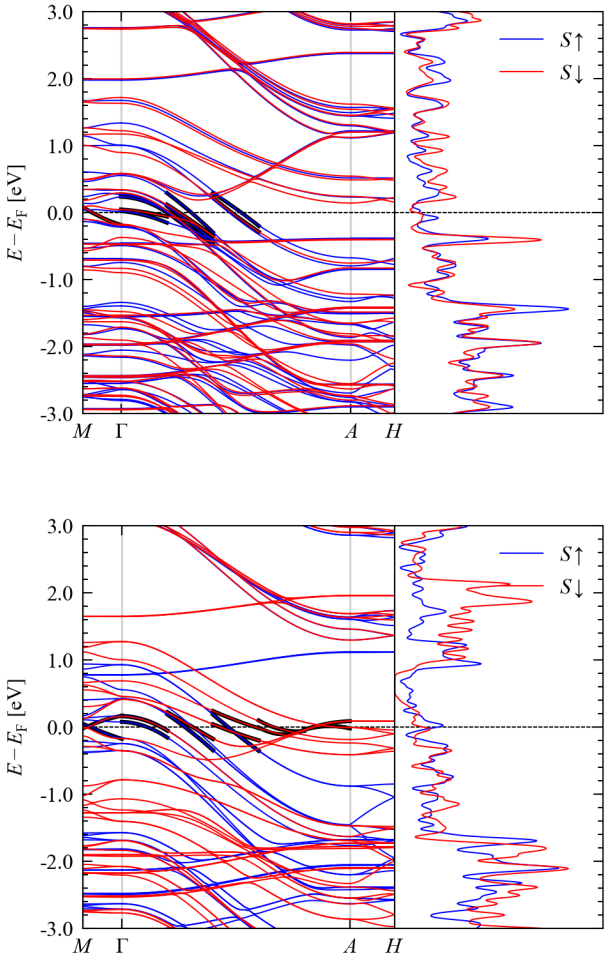

Figure S17. Band dispersion and electronic density of states (DoS) curves of the Co analogue of the **FeTHT** framework calculated with PBEsol (top) and PBEsol+U with a Hubbard correction of U = 5 eV applied to the Fe d states (bottom). As in Figure S5, the blue and red colours denote electronic states in the two spin channels, and the thick black lines indicate parts of the dispersion used to evaluate $\partial^2 E(k)/\partial k^2$ for estimating the carrier effective masses.

Table S5. Peak parameters to fit Fe^{2+} and Fe^{3+} multiplets in **FeTHT**. The reference parameters are of Fe_3O_4.[4] Fe_3O_4 has a mixed $Fe^{3+/2+}$ valency with a 2:1 ratio, which is comparable to the **FeTHT** and thus, the primary reason for reference in fitting the Fe 2p region. Details of the fitting can be found in the table below. Peak 1 represents the lowest binding energy peak for both the Fe^{2+} and Fe^{3+} multiplets. Note that the single Fe^{3+} satellite (~716 eV) is not in the table because peak constraints were not held fixed between samples.

	Peak 1 (eV) [FWHM]	%	Peak 2 (eV) [FWHM]	%	$\Delta E_{(peak2-peak1)}$ (eV)	Peak 3 (eV) [FWHM]	%	$\Delta E_{(peak3-peak2)}$ (eV)	Peak 4 (eV) [FWHM]	%	$\Delta E_{(peak4-peak3)}$ (eV)
Fe 2+											
Reference	708.3 [1.2]	41.6	709.3 [1.2]	43.2	1.0	710.4 [1.4]	15.2	1.1			
Pristine	708.2 [1.0]	41.8	709.2[1.6]	43.1	1	710.3 [1.6]	15.1	1.1			
Fe 3+											
Reference	710.2 [1.4]	34.9	711.1 [31.8]	31.8	1.1	712.4 [1.4]	22.6	1.1	713.6 [1.4]	10.8	1.2
Pristine	710.1 [1.6]	35.1	711.2 [1.5]	31.9	1.1	712.3 [1.6]	22.5	1.1	713.5 [1.6]	10.5	1.2
7 Days	710.1 [1.6]	35.1	711.2 [1.5]	31.9	1.1	712.3 [1.6]	22.5	1.1	713.5 [1.6]	10.5	1.2

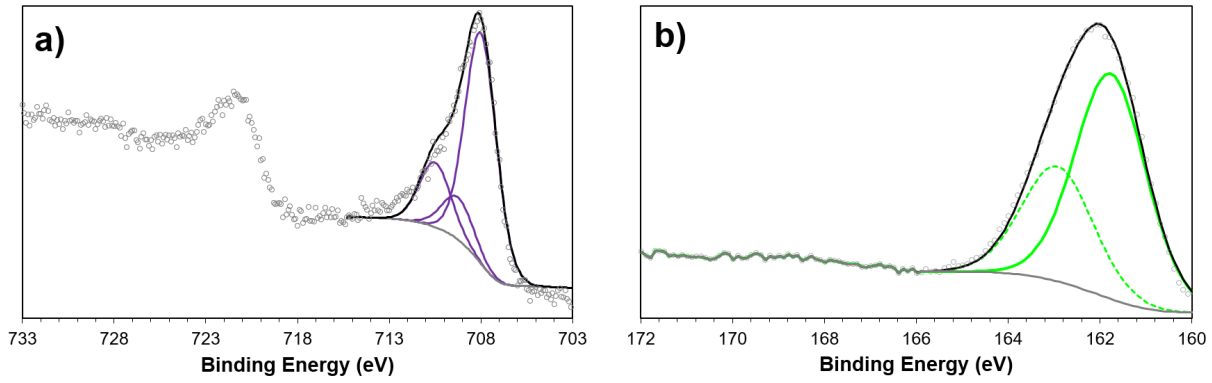

Figure S18. XPS spectra showing the iron 2p (a) and sulfur 2p (b) features from the $[Fe(bdt)_2][HNEt_3]_2$ molecular complex, where bdt = 1,2-benzenedithiolate.

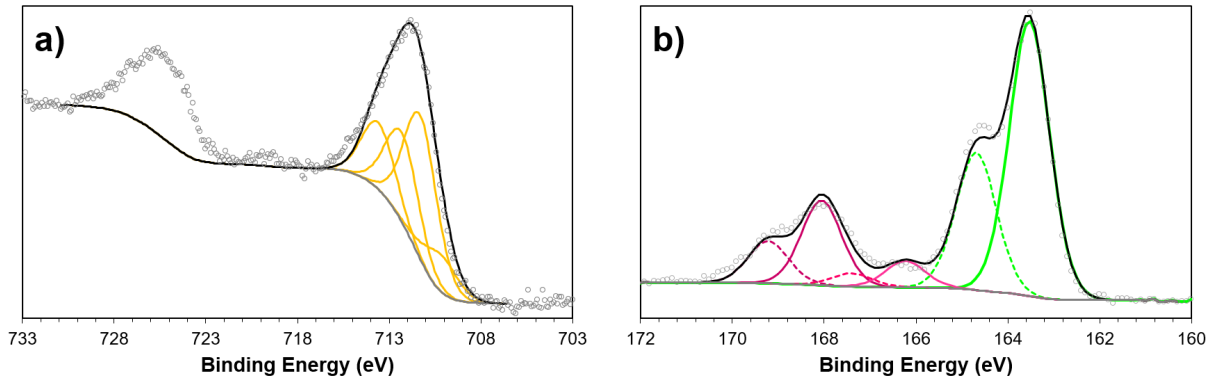

Figure S19. XPS spectra showing the iron 2p (a) and sulfur 2p (b) features from the $[Fe(bdt)_2][HNEt_3]_2$ molecular complex after 3 days of oxidation in air, where bdt = 1,2-benzenedithiolate.

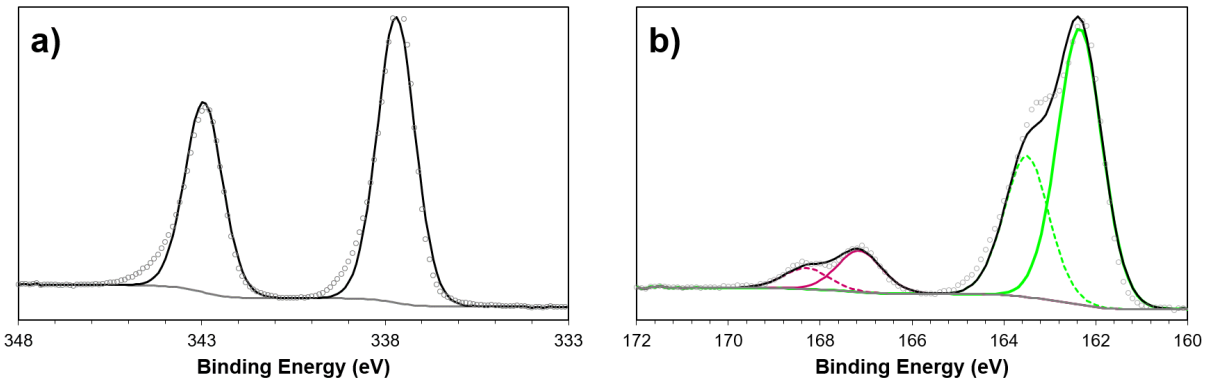

Figure S20. XPS spectra showing the palladium 3d (a) and sulfur 2p (b) features of a $[Pd(bdt)_2]K_2$ molecular complex after 30 minutes of air exposure, where bdt = 1,2-benzenedithiolate.

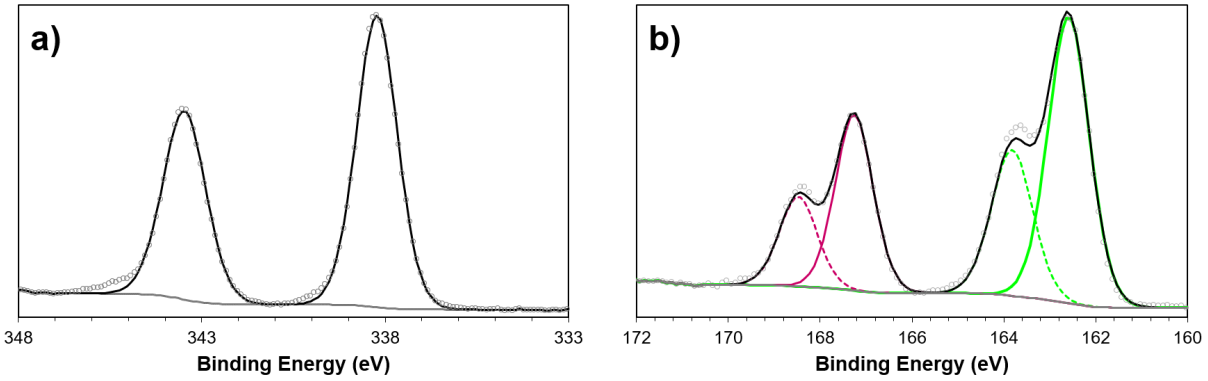

Figure S21. XPS spectra showing the palladium 3d (a) and sulfur 2p (b) features of a $[Pd(bdt)_2]K_2$ molecular complex after 3 days of air exposure, where bdt = 1,2-benzenedithiolate. The molecular formula of this crystalline coordination polymer is $\{[K_4(thf)_4(H_2O)_{2.28}][Pd(O_2SC_6H_4S)_{1.36}(OSC_6H_4S)_{0.64}]_2\}_n$, as reported by Zamora and co-workers.[17]

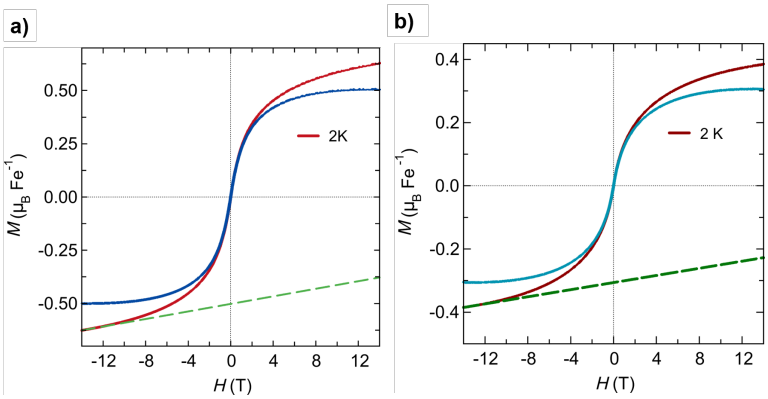

Figure S22. Magnetic hysteresis loops in an **FeTHT** sample exposed to air for three days (a) and pristine **FeTHT** (b).

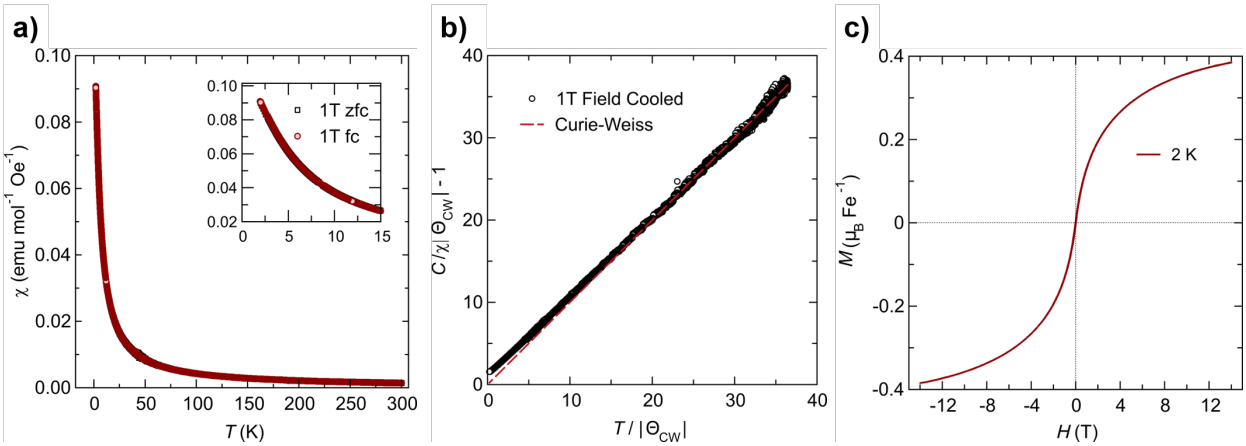

Figure S23. Magnetic studies of pristine **FeTHT**. (*a*) temperature-dependent susceptibility, (*b*) Curie-Weiss fit of the high-temperature region (200–300 K), and (*c*) hysteresis loop collected at 2 K.

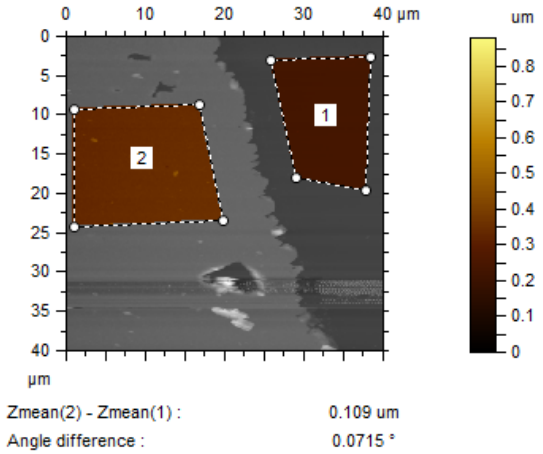

Figure S24. Typical Atomic Force Microscopy (AFM) studies of **FeTHT** films. The measured thickness of the **FeTHT** film is 109(11) nm.

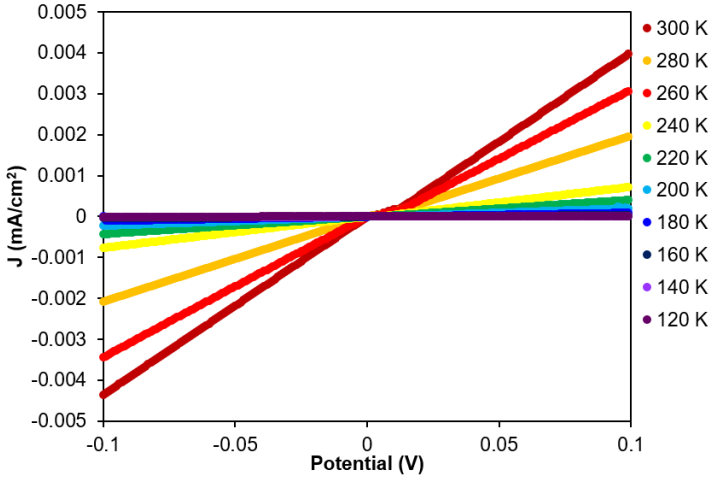

Figure S25. Variable-temperature I-V traces of **FeTHT** demonstrating Ohmic behavior.

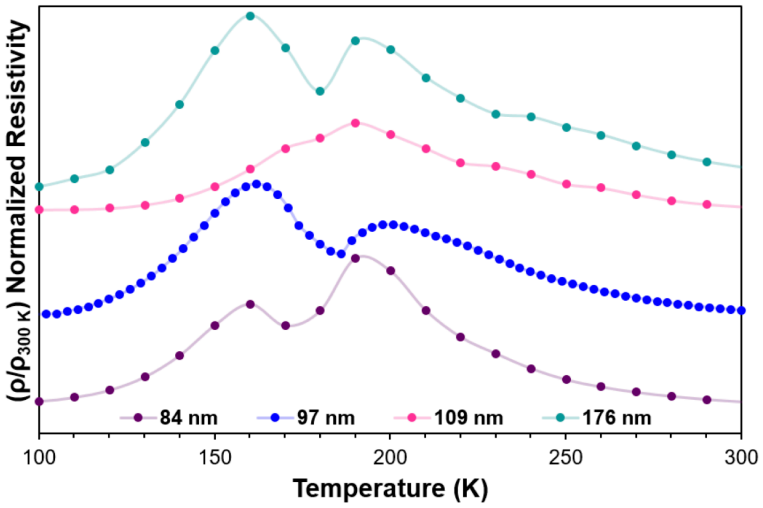

Figure S26. Overlay of the temperature-dependent resistivity data for **FeTHT** films with thicknesses ranging from 84(8) to 176(18) nm.

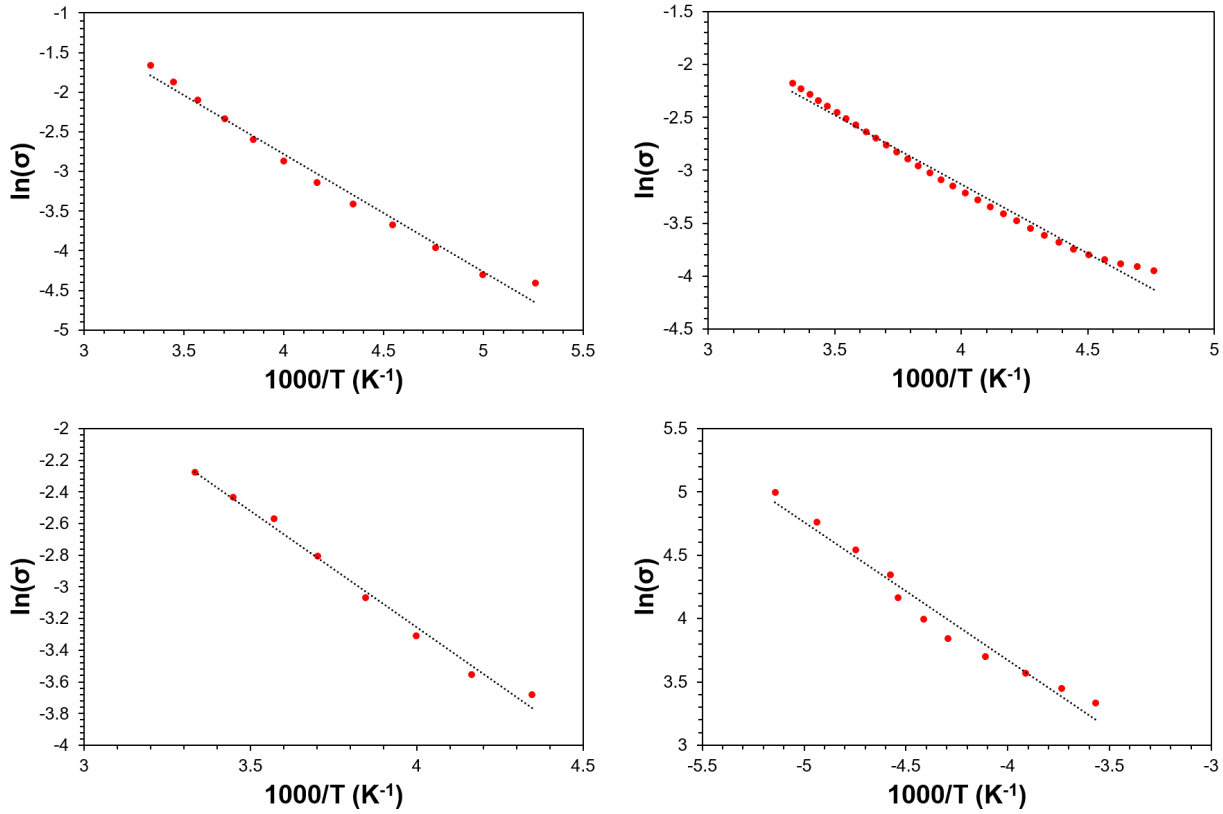

Figure S27. Arrhenius plots for **FeTHT** films with thicknesses of 84(8) nm (top left), 97(10) nm (top right), 109(11) nm (bottom left), and 176(18) nm (bottom right). The data was fit from 300 – 230 K.

Recent DFT studies and a related examination of the temperature-dependent resistivity data for the $Ni_3(HITP)_2$ framework have suggested that the Mott variable-range hopping model best describes the conductivity behaviour of this material.[18] Fitting the high-temperature data for **FeTHT** to the Mott variable-range hopping model and generating an Arrhenius plot gives an activation energy for charge hopping ranging between 6.2 and 8.9 meV (Figure S28; Table S6). Interestingly, these values are similar to the 6 meV hopping barrier reported for the $Ni_3(HITP)_2$ 2D framework. This small activation barrier suggests that defects, likely grain boundaries in the 2D sheets, play a significant role in the transport properties of these 2D MOFs.

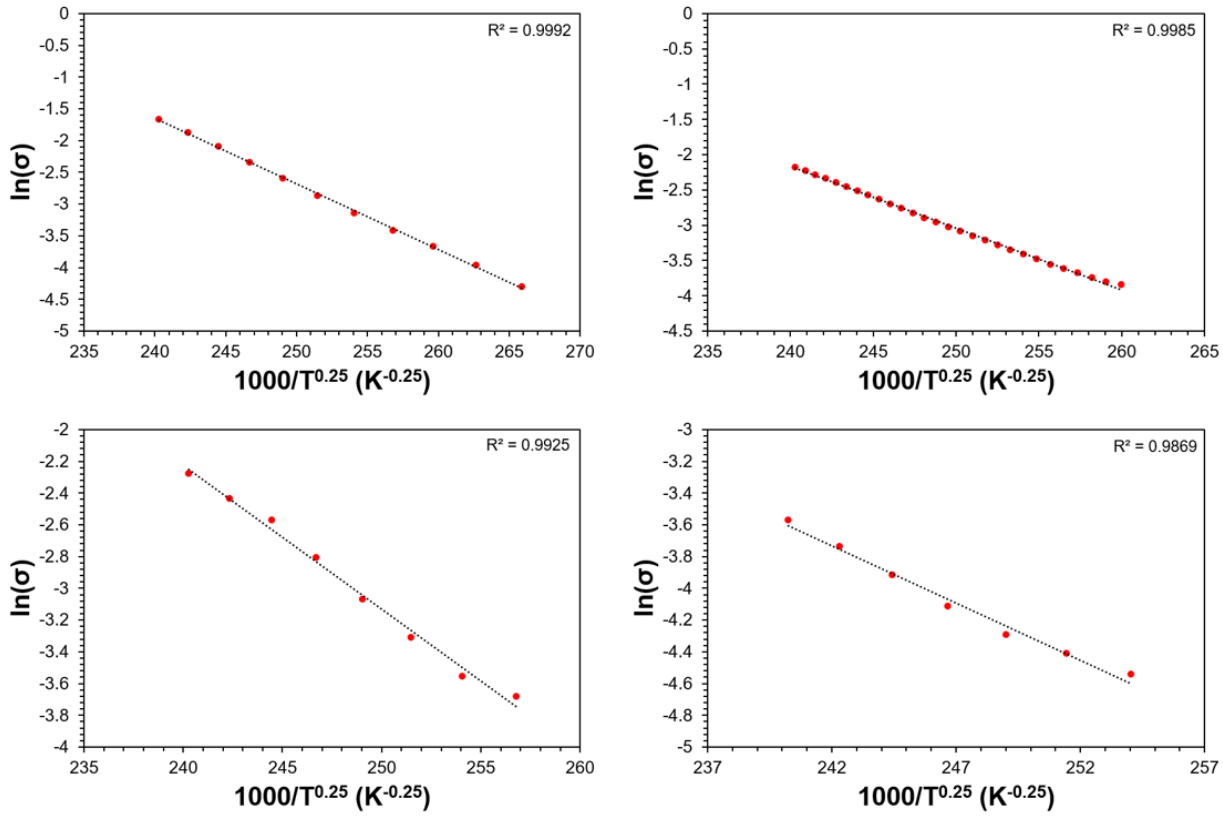

Figure S28. Arrhenius plots using the variable range hopping model for **FeTHT** films with thicknesses of 84(8) nm (top left), 97(10) nm (top right), 109(11) nm (bottom left), and 176(18) nm (bottom right). The data was fit from 300 – 230 K.

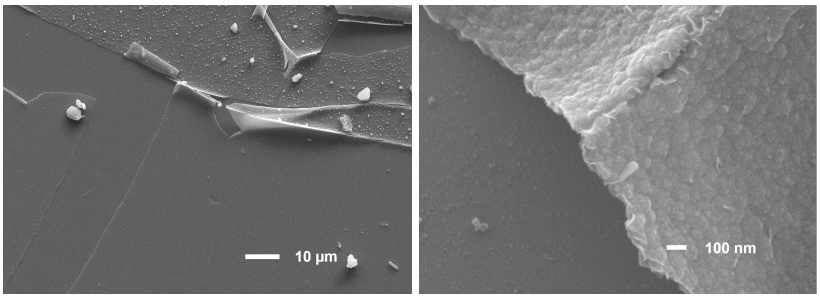

Figure S29. SEM images of **FeTHT** after resistivity studies. (*left*) medium magnification (1000×) and *(right*) high magnification (60,000×).

Table S6: Summary of electrical transport data for **FeTHT** films.

Entry	Thickness (nm)	Conductivity (S/cm) @ 300 K	E_a [a] (meV)	E_a [b] (meV)	$T_{Metallic}$ (K)
1	84(8)	0.3	12.8	8.9	160
2	97(10)	0.1	11.3	7.5	190
3	109(11)	0.1	12.7	7.8	160
4	176(18)	0.03	9.4	6.2	160
5	410(41)	0.02	–	8.5	170

[a] fitted using the Arrhenius equation; [b] fitted using the variable range hopping model.

Table S7: Transport data for an **FeTHT** sample with 275(28) nm thickness after exposure to ambient atmosphere for varying amount of time (from Figure 5).

Air Exposure	**Conductivity (S/cm) @ 300 K**	**$T_{metallic}$ (K)**
as-prepared	0.2	100
2.5 days	0.02	135
1 month	1.4×10^{-3}	265
1.5 months	8.0×10^{-4}	300

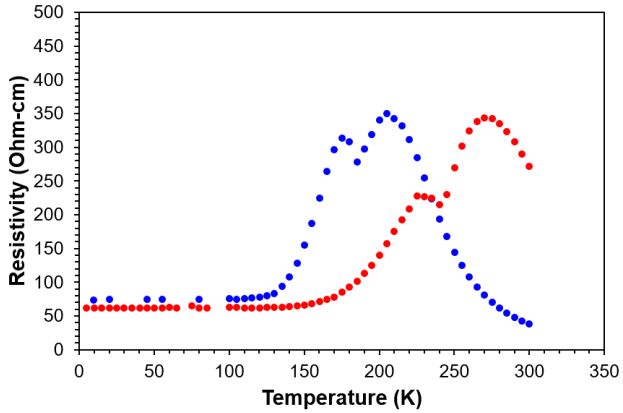

Figure S30. Temperature-dependent resistivity data for a 310(31) nm **FeTHT** film as-prepared (blue) and after 3 days of air exposure at 60°C (red).

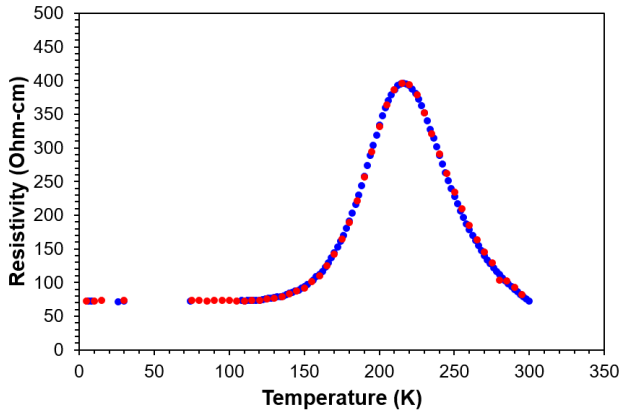

Figure S31. Temperature-dependent resistivity data for a 310(31) nm **FeTHT** film as-prepared (blue) and after 3 days at 60°C under 1 atmosphere of helium (red).

Table S8. Comparison of the structural and physical properties of two FeTHT 2D MOFs

	$Fe_3(THT)_2(NH_4)_3$ (reference 19)	**FeTHT** as-prepared (this work)
Unit cell	a=b= ~1.97 nm c= ~3.3 Å	a=b= ~1.9 nm c= ~3.34 Å
Stacking mode	Inclined AA	Inclined AA
Fe^{2+}	< 0.1 %	67 %
Fe^{3+}	~100 %	33 %
BET surface area	526 m^2/g	370 m^2/g
Transport type	semiconducting	semiconducting / metallic

References:

(1) Sakamoto, R.; Kambe, T.; Tsukada, S.; Takada, K.; Hoshiko, K.; Kitagawa, Y.; Okumura, M.; Nishihara, H. π-Conjugated Trinuclear Group-9 Metalladithiolenes with a Triphenylene Backbone. *Inorg. Chem.* **2013**, *52*, 7411-7416.

(2) Clough, A. J.; Yoo, J. W.; Mecklenburg, M. H.; Marinescu, S. C. Two-Dimensional Metal–Organic Surfaces for Efficient Hydrogen Evolution from Water. *J. Am. Chem. Soc.* **2015**, *137*, 118-121.

(3) Clough, A. J.; Skelton, J. M.; Downes, C. A.; de la Rosa, A. A.; Yoo, J. W.; Walsh, A.; Melot, B. C.; Marinescu, S. C. Metallic Conductivity in a Two-Dimensional Cobalt Dithiolene Metal–Organic Framework. *J. Am. Chem. Soc.* **2017**, *139*, 10863-10867.

(4) Grosvenor, A. P.; Kobe, B. A.; Biesinger, M. C.; McIntyre, N. S. Investigation of multiplet splitting of Fe 2p XPS spectra and bonding in iron compounds. *Surf. Interface Anal.* **2004**, *36*, 1564-1574.

(5) Kresse, G.; Hafner, J. Ab initio molecular dynamics for liquid metals. *Phys. Rev. B* **1993**, *47*, 558(R)-561(R).

(6) Perdew, J. P.; Ruzsinszky, A.; Csonka, G. I.; Vydrov, O. A.; Scuseria, G. E.; Constantin, L. A.; Zhou, X.; Burke, K. Restoring the Density-Gradient Expansion for Exchange in Solids and Surfaces. *Phys. Rev. Lett.* **2008**, *100*, 136406.

(7) Grimme, S.; Antony, J.; Ehrlich, S.; Krieg, H. A consistent and accurate ab initio parametrization of density functional dispersion correction (DFT-D) for the 94 elements H-Pu. *J. Chem. Phys.* **2010**, *132*, 154104.

(8) Dudarev, S. L.; Botton, G. A.; Savrasov, S. Y.; Humphreys, C. J.; Sutton, A. P. Electron-energy-loss spectra and the structural stability of nickel oxide: An LSDA+U study. *Phys. Rev. B* **1998**, *57*, 1505-1509.

(9) Blöchl, P. E. Projector augmented-wave method. *Phys. Rev. B* **1994**, *50*, 17953-17979.

(10) Kresse, G.; Joubert, D. From ultrasoft pseudopotentials to the projector augmented-wave method. *Phys. Rev. B* **1999**, *59*, 1758-1775.

(11) Monkhorst, H. J.; Pack, J. D. Special points for Brillouin-zone integrations. *Phys. Rev. B* **1976**, *13*.

(12) Skelton, J. M. Transformer. **2017**.

(13) Sheberla, D.; Sun, L.; Blood-Forsythe, M. A.; Er, S.; Wade, C. R.; Brozek, C. K.; Aspuru-Guzik, A.; Dincă, M. High Electrical Conductivity in Ni_3(2,3,6,7,10,11-hexaiminotriphenylene)$_2$, a Semiconducting Metal–Organic Graphene Analogue. *J. Am. Chem. Soc.* **2014**, *136*, 8859-8862.

(14) Shick, A. B.; Liechtenstein, A. I.; Pickett, W. E. Implementation of the LDA+U method using the full-potential linearized augmented plane-wave basis. *Phys. Rev. B* **1999**, *60*, 10763-10769.

(15) Sheykhi, S.; Payami, M. Electronic structure properties of UO_2 as a Mott insulator. *Physica C* **2018**, *549*, 93-94.

(16) Wang, L.; Maxisch, T.; Ceder, G. Oxidation energies of transition metal oxides within the GGA + U framework. *Phys. Rev. B* **2006**, *73*, 195107.

(17) Castillo, O.; Delgado, E.; Goḿez-García, C. J.; Hernańdez, D.; Hernańdez, E.; Herrasti, P.; Martín, A.; Zamora, F. i. Comparative Studies of Oxidation Processes on Group 10 Metals Dithiolene Derivatives in the Formation of Coordination Polymers. *Cryst. Growth Des.* **2018**, *18*, 2486-2494.

(18) Foster, M. E.; Sohlberg, K.; Allendorf, M. D.; Talin, A. A. Unraveling the Semiconducting/Metallic Discrepancy in $Ni_3(HITP)_2$. *J. Phys. Chem. Lett.* **2018**, *9*, 481-486.

(19) Dong, R.; Han, P.; Arora, H.; Ballabio, M.; Karakus, M.; Zhang, Z.; Shekhar, C.; Adler, P.; Petkov, P. S.; Erbe, A.; Mannsfeld, S. C. B.; Felser, C.; Heine, T.; Bonn, M.; Feng, X.; Cánovas, E. High-mobility band-like charge transport in a semiconducting two-dimensional metal–organic framework. *Nat. Mater.* **2018**, *17*, 1027-1032.